Low temperature synthesis of new highly graphitized N-doped carbon for Pt fuel cell supports, satisfying DOE 2025 durability standards for both catalyst and support

Ha-Young Lee [a], Ted H. Yu [b], Cheol-Hwan Shin [a], Alessandro Fortunelli [b,c], Sang Gu Ji [d], Yujin Kim [e], Tong-Hyun Kang [a], Byong-June Lee [a], Boris V. Merinov [b], William A. Goddard III [b,*], Chang Hyuck Choi [e,*], Jong-Sung Yu [a,f,**]

[a] *Department of Energy Science and Engineering, Daegu Gyeongbuk Institute of Science & Technology (DGIST), Daegu 42988, Republic of Korea*
[b] *Materials and Process Simulation Center, California Institute of Technology, Pasadena, CA 91125, USA*
[c] *CNR-ICCOM, Consiglio Nazionale delle Ricerche, Pisa 56124, Italy*
[d] *School of Materials Science and Engineering, Gwangju Institute of Science and Technology (GIST), Gwangju 61005, Republic of Korea*
[e] *Department of Chemistry, Pohang University of Science and Technology (POSTECH), Pohang 37673, Republic of Korea*
[f] *Energy Science and Engineering Research Center, DGIST, Daegu 42988, Republic of Korea*

ARTICLE INFO

ABSTRACT

For polymer electrolyte membrane fuel cells (PEMFCs), the state-of-the-art electrocatalysts are based on carbon-supported Pt group metals. However, current carbon supports suffer from carbon corrosion during repeated start-stop operations, causing performance degradation. We report a new strategy to produce highly graphitized carbon with controllable N-doping that uses low-temperature synthesis (650 °C) from g-C_3N_4 carbon-nitrogen precursor with pyrolysis using Mg. The high graphiticity is confirmed by high-intensity 2D Raman peak with low I_D/I_G (0.57), pronounced graphitic XRD planes, and excellent conductivity. Without further post-treatment, this highly graphitized N-doped carbon (HGNC) material combines high pyrrolic-N content with high porosity. Supporting Pt on HGNC exhibits excellent oxygen reduction activity for PEMFC with greatly improved durability as proved by real-time loss measurements of Pt and carbon, the first to surpass the DOE 2025 durability targets for both catalyst and support. The Pt/HGNC-65 shows 32% and 24% drop in mass activity after accelerated durability tests of both electrocatalyst and support, respectively, which are less than DOE target of 40% loss. The atomistic basis for this durability is explained via quantum mechanics-based molecular dynamics simulations. Interestingly, it is found that pyrrolic-N strongly interacts with Pt, making the Pt catalyst more stable during fuel cell reaction.

1. Introduction

PEMFCs constitute a most promising green energy source for many applications due to their high-power density, conversion efficiency, and lack of pollutant emissions. In recent decades, remarkable progress has been achieved in power density and catalyst utilization [1]. To accelerate the sluggish oxygen reduction reaction (ORR) while reducing cost, many investigations have been reported on Pt alloy and non-Pt group metal catalysts [2,3]. However, catalyst activity, durability, and cost remain as formidable challenges for large-scale fuel cell implementation [4–6]. These catalysts are usually supported on highly-graphitic porous carbon, which provides good conductivity, chemical inertness, cost efficiency, and high surface area, while achieving efficient utilization of catalyst nanoparticles (NPs) and maximizing catalyst activity and stability [7].

Unfortunately, a prime cause of performance loss in PEMFCs is carbon support degradation [8,9]. For automotive PEMFCs, carbon degradation is accelerated by repeated start-stop operations, where reduction

---

of oxygen brought into the anode causes oxidation of the carbon support and degradation of the catalyst at cathode with potentials above 1.44 V_{RHE} [10]. At these higher potentials, catalyst NPs detach from the oxidized support, dramatically degrading catalytic activity. Consequently, the properties of the carbon support are crucial in determining fuel cell performance, efficiency, and long-term stability. The three key features most desired in a carbon support for electrolysis are 1) graphiticity for high electronic conductivity and stability, 2) porosity for high surface area and mass transfer, and 3) heteroatom doping for activity and synergistic effects.

The preparation temperature plays a key role in controlling all three features [7]. Usually, graphitic carbons are synthesized by pyrolyzing organic precursors at temperatures > 1000 °C to attain graphiticity [11–13], but most as-prepared carbon materials display low levels of graphiticity unless pyrolyzed at temperatures > 2000 °C [14]. However, because of thermally-induced tight cross-linking, as-prepared carbons at high temperature usually have low porosity, which is detrimental for an effective mass transport [15,16]. Analogously, nitrogen-doping into the carbon has also been shown to provide synergistic effects for ORR [17–19], tuning the electronic structure of the framework while improving both durability and activity of the supported Pt, especially in the form of pyrrolic N-doping sites [20]. However, this pyrrolic-N configuration usually occurs only at low synthesis temperatures (<1000 °C). Since increasing temperature increases graphiticity and conductivity, but decreases both N content and porosity, the optimum control over these key factors in carbon synthesis may not seem possible.

Herein, we develop a novel low-temperature synthesis strategy that provides high surface area and significant N-doping while developing high graphiticity carbon. Our process involves thermal reduction of g-C_3N_4 aided by liquid Mg metal to provide a porous structure without a template. In the range of 650–850 °C, the strongly reducing liquid Mg [21–24] in the presence of Ar or N_2 gas flow reacts with most of the N in g-C_3N_4 framework to generate Mg_3N_2, while the N-deficient g-C_3N_4 cross-links quickly to form highly graphitized carbon. This Mg-aided carbonization occurs at an unprecedented low temperature of 650 °C, thereby maintaining a high level of nitrogen content (favourably with predominant pyrrolic-N character) while developing a highly graphitic framework. Then, post-carbonization acid treatment (etching) dissolves out excess Mg and Mg_3N_2, leaving a highly graphitized N-doped carbon (HGNC) with high porosity. Loading Pt NPs into this HGNC support produces a Pt/HGNC cathode that displays excellent ORR activity along with exceptional durability, far better than commercial Pt/C as proved by accelerated durability tests following US DOE protocols. This enhanced durability is explained by real-time mass loss measurements and quantum mechanics-based simulations.

2. Experimental section

2.1. Synthesis of highly graphitized N-doped carbon (HGNC)

The g-C_3N_4 was synthesized by a reported method [25]. Typically, 30 g of urea was put in a covered alumina crucible and heated to 550 °C with a 3.5 °C min^{-1} heating rate under air atmosphere for 4 h. Such-prepared g-C_3N_4 was confirmed by XRD and then mixed with the same weight of Mg powder. The well-mixed powder was transferred to the alumina crucible, covered, and heated in the flow of Ar or N_2 at 650 ~ 850 °C for 5 h in the tube furnace. The obtained sample was stirred for 5 h in 2 M HCl solution to remove Mg species [21,22]. Then, the sample was filtered by deionized water and dried. The dried sample was denoted as HGNC-X, where X stands for the treatment temperature, i.e. 65 for 650, 75 for 750, and 85 for 850 °C. To test the effect of Mg during the carbonization process, the g-C_3N_4 was also treated under 5% H_2/Ar and Ar at 650 °C identically without Mg. Each sample was named as CNH-65 and CNAr-65, respectively.

2.2. Platinum deposition on HGNC

The homogeneous deposition method with ethylene glycol (HD-EG) was carried out for Pt deposition [26]. Briefly, 50 mg of as-prepared HGNC-X was dispersed in 200 mL of DI water with the desired concentration of H_2PtCl_6 solution for 20 wt% Pt loading. After sonication, urea was added with a molar ratio for Pt and urea of 1:10. The mixture was heated at 90 °C for 1 h and cooled to room temperature. 200 mL of EG was added to the mixture. After stirring for 3 h, the mixed solution was heated at 120 °C for 1 h and stirred overnight. Then, the solution was filtered and washed with water. The obtained samples were dried in an oven at 60 °C. The platinized samples were denoted as Pt/HGNC-X.

2.3. Characterizations

Powder X-ray diffraction (XRD) patterns of the samples were recorded using a Rigaku Smartlab diffractometer with Cu-Kα (λ = 0.15406 nm) operated at 40 kV and 30 mA at a scan rate of 4° min^{-1}. The Fourier transform infrared (FTIR) spectra of samples were recorded on a NICOLET CONTINUUM. High-resolution transmission electron microscopy (HR-TEM) and high-resolution scanning electron microscope (HR-SEM) images were collected using JEOL FE-2010, operated at 300 kV. The scanning electron microscopy (SEM) images were obtained using a Hitachi S-4700 microscope operated at an acceleration voltage of 10 kV. Nitrogen adsorption-desorption isotherms were measured at -196 °C using a Micromeritics ASAP 2460 accelerated surface area and porosity analyser after the samples were degassed at 150 °C to 20 mTorr for 12 h. The specific surface area was determined based on the Brunauer-Emmett–Teller (BET) method from nitrogen adsorption data in the relative pressure range from 0.05 to 0.2. Raman analysis was carried out using a Raman spectrometer (NICOLET ALMECA XR), manufactured by Thermo Scientific. A 532 nm laser beam was used for excitation. The quantitative analysis for C, N, and H was carried by the elemental analyzer (Vario MACRO cube, Elementar). X-ray photoelectron spectroscopy (XPS) was performed using an ESCALAB 250 XPS System with a monochromated Al Kα (150 W) source. The energy scale is aligned by using the Fermi level of the XPS instrument (4.10 eV versus absolute vacuum value). The amount of metal loading in all the samples was measured by thermogravimetric analysis (TGA) using a Bruker TGDTA2000SA analyser. To evaluate the electrical conductivity of samples, a home-made four-probe configuration was used [27]. Non-conductive hollow Teflon cylinder contained the powder sample. The cylinder was sealed by two metal pistons and pressure was applied to the piston. The applied pressures were regulated by depositing known weights on the metal piston. A current is applied to the materials through the metallic pistons. Voltage was collected via leads through the samples in the cylinder. The electronic conductivity (σ) of the samples was calculated by the following equation;

$$\sigma = \frac{l}{RA} \tag{1}$$

where R is the resistance of the sample, A is the cross-sectional area of the sample (0.126 cm^2), and l is the distance between the two voltage probes (0.2 cm).

Contact angle and surface roughness were determined by using a contact angle measurement system (DSA100, KRÜSS) and an atomic force microscope (AFM, PARK NX10), respectively.

2.4. Electrochemical measurements

Electrochemical measurements with a three-electrode system were carried out at room temperature using a rotating disk electrode (RDE) connected to an electrochemical analyser (Biologic VMP3) using Ag/AgCl with saturated KCl and a Pt wire as a reference and counter electrode, respectively. All potentials are reported in terms of reversible

hydrogen electrode (RHE). For this purpose, the Ag/AgCl reference electrode was calibrated with respect to RHE. A glassy carbon RDE with 3 mm in diameter coated with prepared Pt/HGNC-X or commercial Pt/C (20 wt% Pt on ketjen black, Tanaka Kikinzoku Kogyo Co.) was used as a working electrode. The dispersion of 5.0 mg of the corresponding catalyst in a mixture of 0.1 mL 5% Nafion solution (Sigma Aldrich) and 0.9 mL DI water was prepared as a catalyst ink. The dispersed ink was cast over glassy carbon electrode and dried at 60 ℃ in an oven. A Pt loading on electrode was about 5 µg cm^{-2}. All electrochemical tests were processed at room temperature. The cyclic voltammetry (CV) experiments were performed in N$_2$-saturated 0.1 M HClO$_4$ solution for ORR with a scan rate of 50 mV s^{-1} in the potential range from 1.1 to 0.05 V in acid medium. Electrochemical surface area (ECSA) was calculated by following equation [28];

$$ECSA\,(m^2\quad g^{-1}) = \frac{Q_H\quad(uC\quad cm^{-2})}{[Pt]\quad g\quad m^{-2}\quad \times\quad 210\quad uC\quad cm^{-2}} \tag{2}$$

where [Pt] is loading amount of Pt on electrode, 210 uC cm^{-2} represents the charge required to oxidize a monolayer of hydrogen on Pt theoretically, and Q$_H$ is a total charge of hydrogen desorption which is calculated from CVs in N$_2$-saturated 0.1 M HClO$_4$.

RDE measurements were also performed by recording linear sweep voltammetry (LSV) curves in the O$_2$-saturated 0.1 M HClO$_4$ solution. The LSV curves for ORR at 1600 rpm were recorded between + 1.0 and − 0.2 V in acid medium at a potential scan rate of 10 mV s^{-1}, where the Pt ring potential was measured at a set potential of + 1.1 V. The accelerated durability test (ADT) for electrocatalyst was carried out by 30k CV cycles in N$_2$-saturated HClO$_4$ solution between 0.6 and 0.95 V$_{RHE}$ with a scan rate of 100 mV s^{-1}. The LSV curves were obtained before and after ADT. The kinetic current for Tafel plot was calculated from mass transport correction of LSV curve by Koutecky-Levich equation below;

$$j_k\quad(mA\quad cm^{-2}) = \frac{j\quad(mA\quad cm^{-2})\quad\times\quad j_d\quad(mA\quad cm^{-2})}{j_d\quad(mA\quad cm^{-2})\quad-\quad j\quad(mA\quad cm^{-2})} \tag{3}$$

where j$_k$ is kinetic current density, j is the measured current density, and j$_d$ stands for diffusion limited current density.

2.5. MEA preparation and single cell tests

Membrane electrode assemblies (MEAs) were prepared using the catalyst-coated membrane (CCM) with an active area of 10 cm^2. The commercial Pt/C (Tanaka, 20 wt% Pt on ketjen black) was used as anode catalysts for all the tests. As-synthesized Pt/HGNC-X or commercial 20 wt% Pt/C catalyst was used as an active cathode electrode. All the catalysts inks were composed of 10 mg of catalyst powder, 80 µg of 2-propanol, 70 µg of DI water, and 66 µg of 5 wt% Nafion solution (Sigma Aldrich). 360 µL of well-dispersed catalyst slurry is directly sprayed onto a Nafion N211 membrane with an active area of 10 cm^{-2} by using air spray gun so as to have a loading amount of 0.5 mg$_{catalyst}$ cm^{-2}, and the prepared CCMs were dried at 60 ℃ for 6 h. The catalyst loading on each electrode was 0.10 mg$_{Pt}$ cm^{-2}. The MEAs were assembled with commercial gas diffusion layers (GDL, SGL 39 BCE) without hot-pressing. PEMFC performance was measured at 80 ℃ where fully humidified H$_2$ and O$_2$ (or Air) were supplied to the anode and cathode at a flow rate of 300 and 1000 mL min^{-1}, respectively. Back-pressure was maintained as 0.5 bar during the test process. The polarization curves for MEAs were obtained under constant current by electronic load (PLZ664WA, Kikusui) with PEMFC test station (Scitech Inc., Korea). Electrochemical impedance spectroscopies (EIS) were performed from 5 kHz to 100 mHz at a cell current of 100 mA cm^{-2}. Back-pressure was maintained as 0.5 bar during the test process.

To assess the durability of catalysts, an accelerated durability test (ADT) was carried out based on electrocatalyst cycles and catalyst support cycles suggested by the Department of Energy (DOE) [29].

According to electrocatalyst cycle protocol, the square voltage cycling tests were conducted between 0.6 V and 0.95 V with a hold-time of 3 s at both potentials. After 10, 20, and 30 K cycles, polarization curves, CVs, and EIS were measured. For catalyst support cycles, the triangle voltage cycling tests with a scan rate of 500 mV s^{-1} were performed between 1.0 V and 1.5 V. After 5 K cycles, polarization curves, CVs, and EIS were obtained.

The chronopotentiometry was performed for stationary application. The potential at a fixed 1 A cm^{-2} was recorded for 100 h at 80 ℃, and fully humidified H$_2$ and O$_2$ were supplied to the anode and cathode at a flow rate of 300 and 1000 mL min^{-1}, respectively. Back-pressure was maintained as 0.5 bar during the test.

2.6. Online EFC/ICP-MS and EFC/DEMS analyses

The dissolution of Pt was monitored using ICP-MS (iCAP RQ, Thermo-Fisher Science) coupled with a home-made electrochemical flow cell (EFC). The EFC is comprised of a U-shaped channel with an opening diameter of 3 mm for connection with the working electrode (A-002012, Bio-Logic). The graphite tube counter and Ag/AgCl reference electrodes were connected to the inlet and outlet of the EFC, respectively. An Ar-saturated electrolyte flowed at 400 µL min^{-1} into the EFC inlet and mixed with the internal standard solution containing 5 ppb ^{187}Re and 0.5 M HNO$_3$ (mixing ratio of 1:1) through an Y-shaped connector before entering into the ICP-MS. The dissolved Pt was quantitatively estimated by measuring ^{195}Pt signal against the ^{187}Re. The electrochemical protocol for the online ICP-MS experiment consists of 50 fast CV cycles (200 mV s^{-1}) as a pretreatment step with subsequent 5 slow CV cycles (5 mV s^{-1}) from 0.05 to 1.2 V$_{RHE}$. The potential was hold at 0.05 V$_{RHE}$ after the pretreatment step to stabilize the ICP-MS signal. The catalyst ink for the ICP-MS study was prepared by dispersing 5 mg catalyst in an aqueous solution containing 1179 µL of deionized water, 50 µL of 5 wt% Nafion and 186 µL of isopropanol. The ink was dropcasted onto a glassy carbon (0.071 cm^2) of the working electrode with a target Pt loading of 30 µg cm^{-2}.

The degradation of carbon support was monitored using online differential electrochemical mass spectroscopy (DEMS) (Max 300 LG, Extrel) coupled to an EFC. The EFC has an opening diameter of 10 mm at the bottom of the cell, enabling contact with the working electrodes (A-011169, Bio-Logic). Reference electrode, and graphite tube counter electrodes connected with the EFC outlet to preclude the possible contaminations. The deaerated electrolyte flowed at 70 µL min^{-1} into the EFC inlet, using a syringe pump (TYD01–01, LEADFLUID). The porous PTFE membrane, which is located approximately 100 µm above the working electrode, enables the introduction of volatile products to the mass spectrometer. The signal of CO$_2$ (m/z = 44) was displayed with an arbitrary unit due to uncertainty of its calibration47. The potential program for DEMS study was comprised of 50 fast CV cycles (200 mV s^{-1}, 0.05 −1.2 V$_{RHE}$) and following 5 slow CV cycles (5 mV s^{-1}) in the potential range of 0.05–1.5 V$_{RHE}$, with the potential hold of 5 min at the interim to stabilize the signal. For DEMS study, the catalyst ink was drop-casted onto the glassy carbon (0.071 cm^2) of the working electrode with a target carbon loading of 200 µg cm^{-2}.

2.7. Computational methods

In this study, we first calculated the free energy as a function of the net number of electrons on the surface F(n) using the Perdew-Burke-Ernzerhof, with D3 Dispersion (PBE-D3) [30,31] flavour of QM at different charges, n. Then we determined the grand canonical potentials (GCPs) as a function of applied potential, GCP (n, U), based on the Legendre transformation [32,33].

$$GCP(n, U) = F(n) - ne(U_{SHE} - U) \tag{4}$$

Plotting GCP (n, U) for three or more n, leads to a parabola, for which the minimum is GCP (U). For each geometry, we calculated four

different charges (0 +½, +1, +2) in order to determine the potential dependent energies. Three charges are needed to determine the coefficients, but four charges are recommended to test the validity of the quadratic fit.

The geometries were optimized using the SeqQUEST DFT [34,35] code that uses Gaussian basis sets rather than plane waves. Up-spin orbitals were optimized independently of the down-spin orbitals (spin unrestricted DFT). We used small core angular momentum projected pseudopotentials so that Pt has 18 electrons treated explicitly. The K-points are selected to be $2 \times 2 \times 0$ for structure relaxation and energy calculations. The unit cell dimensions are optimized as $12.3 \times 12.3 \times 26.5$ Å.

Single point energies were calculated with jDFTx using the CANDLE solvation model to obtain free energy as a function of applied potential, U [36,37]. Using this scheme, $\mu_{e,SHE} = 4.66$ eV for all structures. A kinetic energy cutoff of 18 Hartree is used for the wavefunction, and a k-point mesh of $2 \times 2 \times 1$ is used. The unit cell dimensions are $12.3 \times 12.3 \times 18.5$ Å. The following examples show the determination of GCP(U) for graphene surface (Fig. S24). The coordinates for the optimized structure are at the end of the Supplementary Information.

3. Results and discussion

3.1. Synthesis of HGNC-X

A schematic illustration of the synthesis from urea and XRD characterization of the products at each step are shown in Fig. 1a, b, respectively. In the HGNC prepared at 650 °C (HGNC-65), an intense diffraction (002) signal develops at 26° as typical of graphite. This dramatic structural change was confirmed by Raman spectroscopy (Fig. 1c) that exhibits strong G and 2D Raman peaks characteristic of graphite and graphene but no observable signals from g-C_3N_4 - an unusual feature for a low 650 °C carbonization temperature [25]. The ratio (I_D/I_G) of disorder-induced D-peak to symmetry-allowed G-peak as an estimate of framework disorder illustrates very low $I_D/I_G = 0.57$, indicating that HGNC-65 is highly graphitized carbon. The high-intensity 2D signal at 2690 cm^{-1} can be observed only in exceptionally high-graphitized carbon with low lattice defects. All HGNC-X samples prepared at 650–850 °C show the strong (002) peak at 26° in XRD (Fig. S1a) and high-intensity G and 2D peaks in the Raman spectra (Fig. S1b), increasing and narrowing as the carbonization temperature increases (Table S1). Also, when the heating time increases from 1 to 8 h, intensity of the (002) XRD peak and G and 2D Raman signals become higher and narrower (Fig. S2). Especially, the full width at half maximum of 2D signal can be used to estimate the number of carbon layers [38]. The number of layers is reduced with increasing
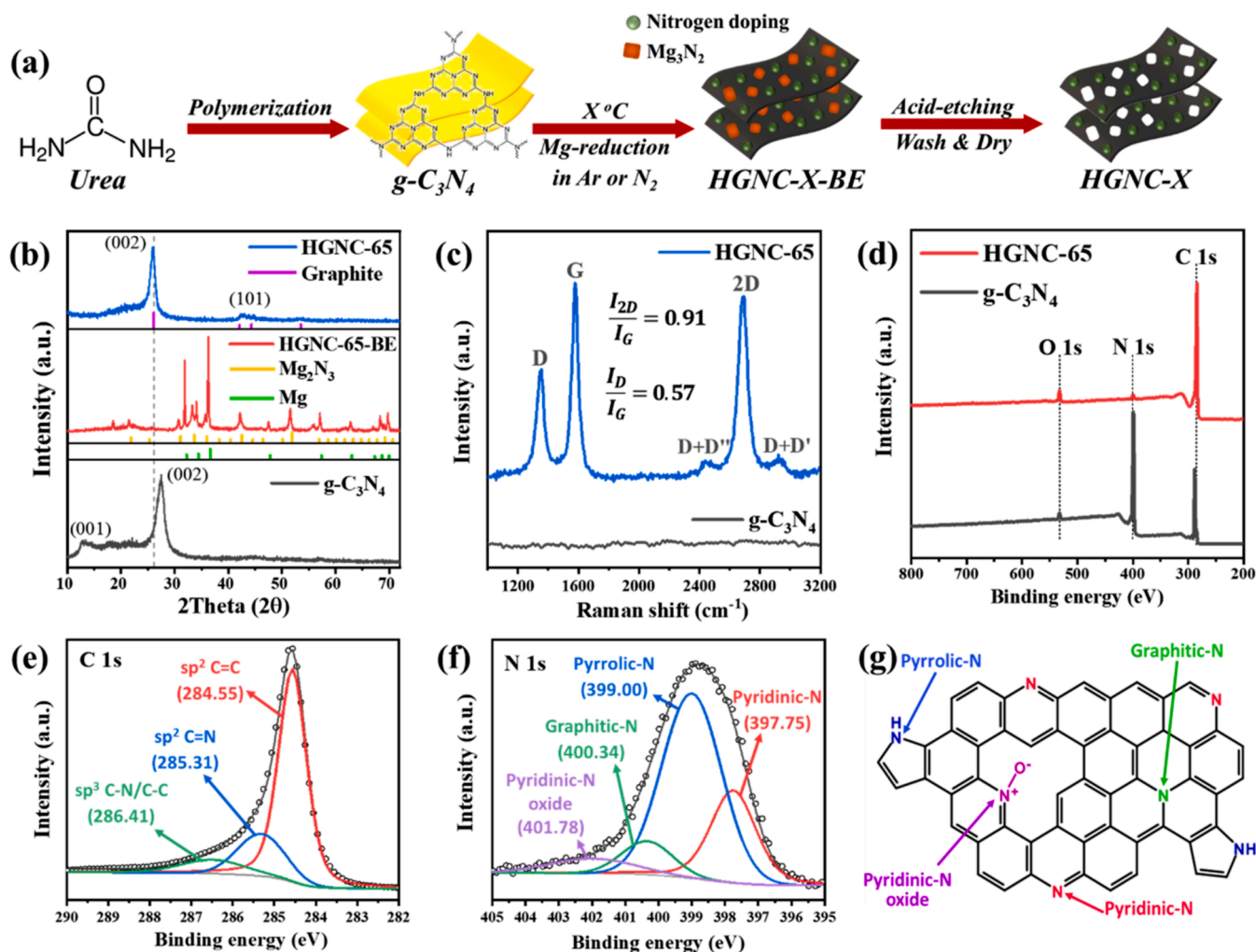

Fig. 1. (a) Scheme for preparation of HGNC-X, (b) XRD profiles of products at each synthesis step for HGNC-65, (c) Raman spectroscopy profiles, and (d) XPS survey scans of HGNC-65 and g-C_3N_4. Corresponding high-resolution XPS spectrum for (e) C 1 s and (f) N 1 s (g) Schematic representation of N sites in HGNC-65.

carbonization temperature and time in HGNC-X samples (Table S1). Due to different treatment conditions in earlier works [23,24], the carbons produced from g-C$_3$N$_4$ were not fully graphitized with much less pronounced graphitic (002) XRD planes and higher I$_D$/I$_G$ values.

To assess the effect of Mg in the carbonization process, we treated g-C$_3$N$_4$ with Ar and 5% H$_2$/Ar without Mg at 650 °C. The resulting CNAr-65 and CNH-65 exhibit XRD and FT-IR spectra similar to the parent g-C$_3$N$_4$ (Fig. S3). Also, CNAr-65 and CNH-65 maintain the yellowish color typical of the original g-C$_3$N$_4$, whereas HGNC changes color from light grey to black (Figs. S4, S5). With increasing temperature, the decomposition gets more severe with CNAr-85 and CNH-85 (Fig. S5a), producing gases and small fragments of C$_x$N$_y$, with no carbonized product remaining. Thus, simple heat treatment in inert conditions cannot convert g-C$_3$N$_4$ to graphitic materials like HGNC-X. To prevent decomposition into gaseous cyano fragments (C$_x$N$_y$), the nitrogen must be removed from g-C$_3$N$_4$, which cannot be achieved by normal heat treatments. In contrast, our method has Mg at its melting temperature (650 °C) to react with nitrogen from g-C$_3$N$_4$ to generate Mg$_3$N$_2$, as confirmed by XRD before HCl etching (HGNC-65-BE) (Fig. 1b). The remaining sp^2 or sp^1 hybridized carbons then quickly reorganize to form a graphitic structure.

X-ray photoelectron spectroscopy (XPS) spectra indicate that the atomic percentage of N is 50.9 at% for g-C$_3$N$_4$ and 2.7 at% for HGNC-65 (Fig. 1d, f and Table S2). The high-resolution C 1 s spectrum exhibits three peaks at 284.55, 285.31, and 286.41 eV (Fig. 1e). The main peak at 284.55 eV is assigned to graphite-like sp^2 C from C=C. The peak at 285.31 eV corresponds to sp^2 C bonded to N as C=N, while the peak at 286.41 eV is assigned to sp^3 C from C-C single bonds [39]. The high-resolution N 1 s XPS spectra (Fig. 1f) deconvolutes into four peaks: pyridinic-N at 397.75 eV (25.5%), pyrrolic-N at 399.00 eV (58.7%), graphitic-N at 400.34 eV (9.1%) and pyridinic-N oxides at 401.78 eV (6.7%) [19,39] (Table S3). N-doping helps to improve the activity of Pt toward ORR. Especially, pyridinic-N is well known to improve ORR kinetics. Furthermore, there are also some studies, where pyrrolic-N could improve ORR catalytic activity [40–42]. Both pyrrolic-N and pyridinic-N have planar N-configurations based on sp^2 hybridized-N. The planar N species have lone pair electrons in perpendicular p-orbital, leading to better electronic conductivity than graphitic-N [43]. Thus, both pyrrolic-N and pyridinic-N in HGNC-65 may help to improve ORR kinetics.

XPS results for other HGNC samples are shown in Fig. S6. As the synthesis temperature increases, the total N content and the pyrrolic-N components decrease (Table S3), with HGNC-85 possessing 1.3 at% N and only 28% pyrrolic N while pyridinic-N becomes predominant at 38.4%. Also, nitrogen and pyrrolic N contents decrease with the carbonization time increases as shown in Fig. S7 and Table S3.

Mg has dramatic effects on porosity and graphiticity of carbon. Pristine g-C$_3$N$_4$ has a sheet-like structure that is maintained for HGNC-65 prepared at 650 °C pyrolysis followed by acid etching (Fig. 2). Before acid etching, carbon sheets mix with Mg and Mg$_3$N$_2$ particles (Fig. S9), that are dissolved by adding 2 M HCl solution, leaving behind mesopores and macropores on the graphitic carbon. Pores of about 50–100 nm are observed on the carbon sheet (Fig. 2b, f), which are more numerous as the carbonization temperature increases to give honeycomb-like porous structures (Fig. 2g, h) beneficial for electron transfer in electrochemical reactions. The HGNC-65 has the largest BET surface area, 375.6 m^2 g^{-1}, while HGNC-85 has the smallest, 288.7 m^2 g^{-1}. The N$_2$ isotherm curves are shown in Fig. S10 with the results in Table S4.

3.2. Electrochemical performance and PEMFC durability tests

The electronic conductivity was measured by four-probe methods (Fig. 3a). The conductivity increases with growing pressure and treatment temperature, indicating increasing graphiticity. All HGNC-X samples show higher conductivity than Vulcan carbon and KB-EC600JD, a well-known highly conductive carbon. The HGNC-65–8 h has slightly higher electrical conductivity than HGNC-65 (prepared by 5 h, Fig. S11a), but has much lower BET surface area and meso porosity for fuel cell reaction. In contrast, CNAr-65 and CNH-65 show almost no conductivity, like pristine g-C$_3$N$_4$ (Fig. S11b).

Linear sweep voltammetry (LSV) and cyclic voltammetry (CV) measurements were performed by the rotating disk electrode (RDE) method (Fig. 3b, d). All the Pt-loaded catalysts have almost identical 20 wt% Pt loading as confirmed by TGA (Fig. S12). g-C$_3$N$_4$, CNAr-65, and CNH-65 are almost ORR inactive even after Pt deposition (Fig. 3c) because of negligible conductivity. In contrast, the Pt/HGNC-X samples exhibit higher onset and half-wave potentials compared to state-of-the-
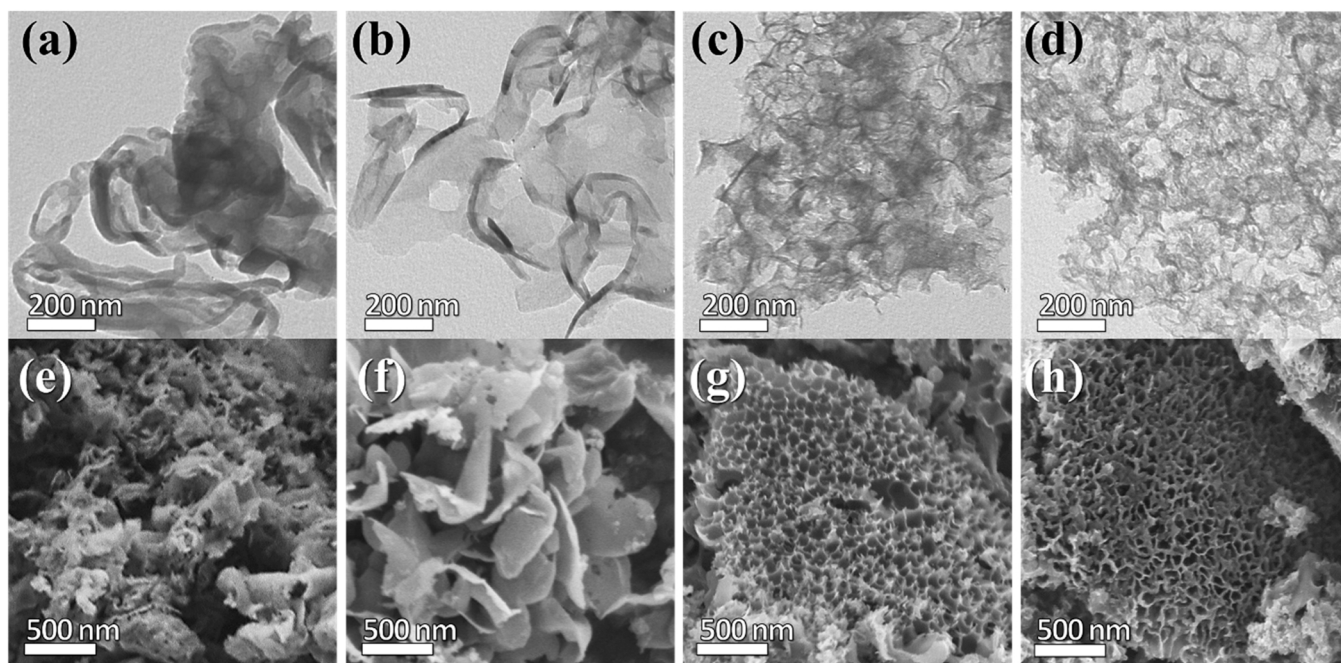

Fig. 2. TEM and SEM images for (a, e) g-C$_3$N$_4$, (b, f) HGNC-65, (c, g) HGNC-75, and (d, h) HGNC-85.
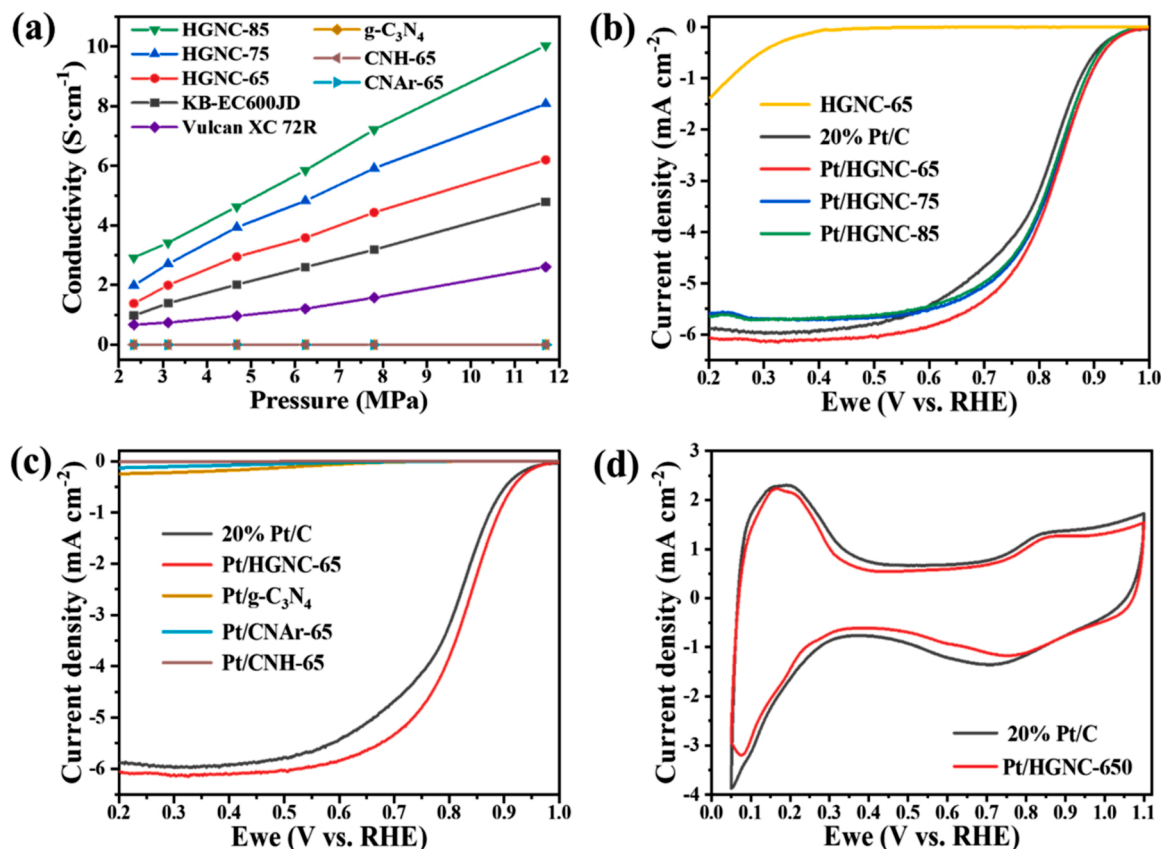
Fig. 3. (a) Electronic conductivity versus pressure profiles of as-prepared samples and commercial carbons. (b-c) ORR polarization curves obtained in O_2-saturated 0.1 M $HClO_4$. (d) Cyclic voltammetry curves of Pt/C and Pt/HGNC-65 in a N_2-purged 0.1 M $HClO_4$ solution at a scan rate of 50 mV s^{-1}.

art commercial Pt/C (20 wt%, Tanaka). The Pt/HGNC-65 has the highest diffusion limited current density, and N_2-purged CVs indicate that Pt/C and Pt/HGNC-65 have similar H_2 desorption and adsorption

areas (Fig. 3d) [28,44]. Electrochemical surface area (ECSA) was determined to be 57.2 and 55.7 m^2 g$_{Pt}^{-1}$ for commercial Pt/C and the Pt/HGNC-65, respectively from N_2-purged CVs. Pt NPs are
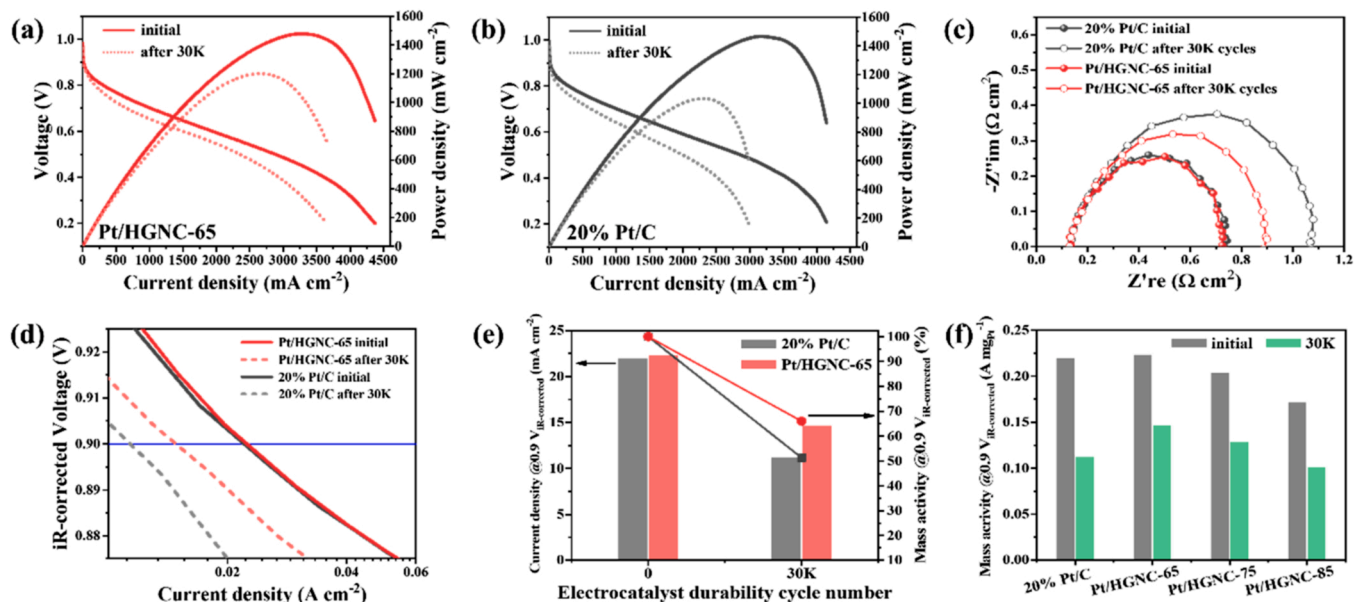

Fig. 4. Single cell polarization and power density curves for (a) Pt/HGNC-65 and (b) commercial 20% Pt/C before and after 30 K cycles of accelerated durability test (ADT) for electrocatalyst durability. (c) Electrochemical impedance spectroscopy (EIS) profiles at a 100 mA cm^{-2} before and after 30 K cycles of the ADT. (d) iR-corrected V-i curves calculated from corresponding polarization curve. (e) Current density and mass activity retention at 0.9 V$_{iR-corrected}$. (f) Mass activity at 0.9 V$_{iR-corrected}$ for commercial Pt/C and Pt/HGNC-X before and after 30 K ADT. The polarization curves and EIS of MEAs were tested at 80 ℃ with fully humidified H_2/O_2 and backpressure as 0.5 bar.

well-distributed over carbon support in both materials (Figs. S14a, d), but Pt/HGNC-65 has larger particle size (~2.2 nm) than commercial Pt/C (~1.8 nm) as shown in Fig S14, which may be the reason for lower ESCA of the former. Even with the low ECSA value, Pt/HGNC-65 has better kinetics toward ORR as shown in Tafel plot (Fig. S13a). The Tafel slopes were calculated in the potential range from 0.93 to 0.90 V_{RHE}. Pt/HGNC-65 shows lower slope (70.5 mV dec^{-1}) than 20% Pt/C (75.4 mV dec^{-1}), indicating better efficiency probably from N-doping and mesoporosity of HGNC-65. Pt/HGNC-65 has smaller Pt NPs compared to Pt/HGNC-75 and Pt/HGNC-85 (Figs. S14 and S15). HGNC-65 was chosen as a representative supporting carbon among the HGNCs prepared at 650 °C for different carbonization time because Pt/HGNC-65 showed the best activity compared to other Pt/HGNC-65-Yh.

We fabricated a membrane electrode assembly (MEA) with commercial Pt/C and with as-prepared Pt/HGNC-65 as the cathode catalyst for single cell test. Accelerated durability tests (ADTs) were carried out to examine stability of electrocatalyst according to US DOE protocols [29]. The potential was cycled between 0.6 and 0.95 V_{RHE}, known to be the potential region for Pt or alloy metal dissolution [45,46] but with little carbon support degradation according to DOE (Fig. S16a). Initially, Pt/HGNC-65 displayed a maximum power density (P_{max}) of 1480 while commercial Pt/C displayed 1465 mW cm^{-2} (Fig. 4a, b), but the Pt/C shows a much more rapid decline than Pt/HGNC-65. After 30 K cycles for Pt/C, P_{max} decreases to 1030 mW cm^{-2} (70% of the initial value) and the mass activity measured at 0.9 $V_{iR-corrected}$ decreases from 0.220 to 0.113 A mg^{-1} (49% decrease), whereas for Pt/HGNC-65, P_{max} decreases to 1200 mW cm^{-2} (81% of the initial value) and the mass activity decreases from 0.217 to 0.147 A mg^{-1} (32% decrease) (Fig. 4d, e).

Figs. S14b, e show TEM images and Pt particle size distribution histograms for commercial Pt/C and Pt/HGNC-65, respectively, after 30 K cycles. The Pt NP size increases during the ADT from 2.2 to 2.6 nm for Pt/HGNC-65, but more noticeably from 1.8 to 3.9 nm for commercial Pt/C, reflecting the activity loss for them.

The ADT polarization curves of MEAs for Pt/HGNC-75 and Pt/HGNC-85 samples are shown in Fig. S17 and Table S5 summarizes the results. Pt/HGNC-65 leads to the most stable Pt NPs compared to the other catalysts (Fig. 4 f). The mass activity at 0.9 $V_{iR-corrected}$ decreases

by only 32% during ADT cycling, compared to the 2025 DOE target of < 40% loss of initial activity. All these results demonstrate that the Pt/HGNC-65 has much better catalyst durability compared to the state-of-the-art Pt/C.

Similar durability tests were also conducted by 30 K cycles of CV between 0.6 and 0.95 V_{RHE} in half cell reaction. Figs. S13b and c demonstrate Pt/HGNC-65 has much better stability than commercial catalyst. The change in half-wave potential ($\Delta E_{1/2}$) for the Pt/HGNC-65 is only 33 mV, while the Pt/C lost 52 mV from initial value.

The chronopotentiometric stability tests were also carried out for 100 h at at a high current density of 1 A cm^{-2}. The commercial Pt/C loses 9.1% of its initial voltage, while the Pt/HGNC-65 drops slightly with 1.8% loss (Fig. S13d). This indicates that Pt/HGNC-65 is highly durable for the staionary PEMFC application as well.

To evaluate the durability of HGNC as a catalyst support, we carried out 5 K ADT cycles with fresh MEAs in the higher potential range between 1.0 and 1.5 V (Fig. 5, S16b) [29]. During the ADT, the carbon supports get oxidized because of the high applied voltage, causing Pt NP agglomeration and detachment [47,48]. The interface between carbon support and Pt degrades heavily during the ADT due to electrochemical actuation processes, further aggravating the durability issues in PEMFC cathode catalysts. It also leads to collapse of the porous carbon morphology, ionomer distribution, and electron pathway, resulting in a dramatic decay of performance due to mass transport and electronic resistance [49,50]. In both Pt/HGNC and Pt/C, power density decreases after the support ADT (Fig. 5a, b). The mass activity drop at 0.9 $V_{iR-corrected}$ is 24%, satisfying the DOE target of < 40% loss of initial value [29]. In contrast, the commercial Pt/C support mostly decomposes to 13.6% of initial activity under the same harsh oxidative condition (Table S6).

We also carried out studies under H$_2$/air conditions. The change in mass activity at 0.9 $V_{iR-corrected}$ demonstrates high durability of Pt/HGNC-65 with loss of 27.1%, while loss of 100% from initial value for Pt/C after 5 K cycles of the carbon ADT (Fig. S18 and Table S7).

For catalyst support ADT, the DOE standard is for only 5 K potential cycles. We extended this to 10 K to verify the dramatic robustness of HGNC-65. The iR-corrected V-i curves after 10 K are displayed in Fig. S19. The mass activity at 0.9 $V_{iR-corrected}$ in Fig. 5e again
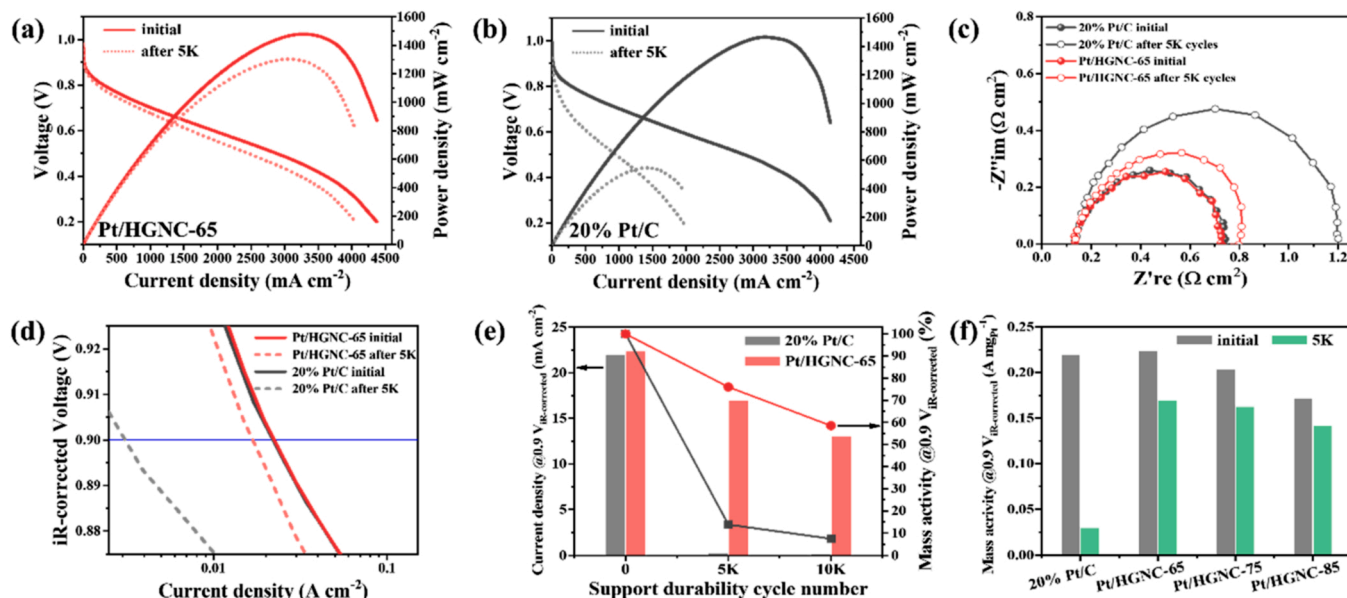

Fig. 5. Single cell polarization and power density curves for (a) Pt/HGNC-65 and (b) commercial 20% Pt/C before and after 5 K cycles of accelerated durability test (ADT) for support durability. (c) Electrochemical impedance spectroscopy (EIS) profiles at a 100 mA cm^{-2} before and after 5 K cycles of the ADT. (d) iR-corrected V-i curves calculated from corresponding polarization curve. (e) Current density and mass activity retention at 0.9 $V_{iR-corrected}$ at each 5 K cycles of ADT. (f) Mass activity at 0.9 $V_{iR-corrected}$ for commercial Pt/C and Pt/HGNC-X before and after 5 K support ADTs. The polarization curves and EIS of MEAs were tested at 80 °C with fully humidified H$_2$/O$_2$ and backpressure as 0.5 bar.

demonstrates superb durability of Pt/HGNC-65, decreasing 41.5% after 10 K, while Pt/C loses 92.3% from its initial value. The final peak Pt NP size for Pt/C is 6.1 nm, over three times larger than the initial size. In contrast, the Pt on HGNC-65 is quite stable with the peak size increasing only by factor 1.5 after 5 K support ADTs, better maintaining their size and distribution (Figs. S14c, f). Aggregation of Pt NPs during carbon corrosion is inevitable [50], but the intrinsic high graphiticity and robustness of HGNC-65 greatly mitigate carbon corrosion and Pt NP aggregation.

To elucidate fundamental origins of the enhanced durability of Pt/HGNC-65, we have monitored its real-time Pt dissolution (electrocatalyst degradation) and carbon corrosion (support degradation) during electrochemical operations. First, the operando inductively coupled plasma-mass spectrometry (ICP-MS) coupled to an electrochemical flow cell (EFC) was used to monitor the Pt dissolution. The potential excursion consists of 50 fast CV cycles (200 mV s^{-1}) as a pretreatment step and subsequent 5 slow CV cycles (5 mV s^{-1}) from 0.05 to 1.2 V$_{RHE}$ (Fig. 6a). In the overall potential protocol, Pt dissolution of Pt/HGNC-65 was much suppressed by less than half compared to that of commercial Pt/C (Fig. 6b, c). A dominant Pt dissolution was found at 0.79 V$_{RHE}$ of cathodic potential scan for Pt/HGNC-65, ca. 30 mV higher than that for Pt/C. This result indicates an efficient reposition of dissolved Pt ions on the HGNC-65 support, probably enabled by introduction of nitrogen functional groups acting as anchoring site for the Pt [51].

In addition, carbon corrosion was studied using an online differential electrochemical mass spectroscopy (DEMS) coupled to EFC by tracking the CO_2 signal ($m/z = 44$). A potential program analogous to the EFC/ICP-MS study, but with a higher upper potential limit (UPL) of 1.5 V$_{RHE}$ at the slow CV cycles, was employed (Fig. 6d). Both Pt/HGNC-65 and Pt/C show a pre-peak (A1$_{carbon}$) at ca. 0.75 in anodic potential scan and an intense carbon corrosion peak (A2$_{carbon}$) as the potential increases, fingerprint signals of Pt-catalyzed and non-catalyzed corrosion of carbon support (Fig. 6e, f) [52,53]. Like the Pt dissolution, the CO_2 evolution signals for the Pt/HGNC-65 are significantly suppressed with ca. 1.8 times less intensity than that for the Pt/C. Therefore, these online spectroscopic analysis data undoubtedly demonstrate a superior durability of both current graphitized carbon support and supported active Pt NPs.

The MEA after catalyst support ADTs was examined by cross-section SEM images (Fig. 7). After 5 K ADT cycles, Pt/HGNC-65 retains the most of catalyst layer on the membrane. The commercial Pt/C displays a dramatic change in the thickness of the catalyst layer from 10.3 to 8.6–3.3–3.2 (after 5 K) and to 1.2–0.36 μm (after 10 K), whereas Pt/HGNC-65 showed only a slight decrease from 7.8 to 7.1–6.7–6.2 μm even after the harsh ADT 10 K cycles, demonstrating the super resistance to oxidative corrosion in accordance with DEMS result [54].

The BET surface area and N content (particularly pyrrolic-N content) decrease while the graphiticity (based on the I$_G$/I$_D$ from Raman spectroscopy) increases as carbonization temperature increases from Tables S1-S4 All Pt/HGNC-X samples are more stable than commercial Pt/C. In particular, Pt/HGNC-65 is the most active and durable catalyst for both electrocatalyst ADT and catalyst support ADT examinations, which may be attributed to its high pyrrolic-N content and high surface area. Fig. S22c and Table S10 show XPS results for N bonding species before and after ADTs. Pyrrolic-N remains as the major N configuration (57.2% and 57.1% in Table S10) after both the electrocatalyst and catalyst support ADTs. Thus, the N species, especially pyrrolic-N, can enhance activity and durability of Pt and carbon structure during the ADTs [20].

To investigate the effect of the HGNC on Pt alloys beyond on pure Pt, common PtCo alloy was prepared and loaded to HGNC-65 and Vulcan XC 72R carbon black (VC). PtCo/HGNC-65 illustrated better performance and durability than PtCo/VC in both in H_2/O_2 and H_2/Air conditions (Fig. S23), clearly indicating the HGNC-65 could be the support material of choice for high performance and durability in PEMFC. Table S11 summarizes the ADT results.

3.3. Quantum mechanics-based analysis

In order to understand the atomistic origins of the high durability of the Pt-HGNC-X catalysts in ORR, we carried out a series of Quantum Mechanics (QM) calculations at the density functional theory (DFT) level using the Perdew-Burke-Ernzerhof functional with the D3 empirical Dispersion correction (PBE-D3) [30,31].

We started with a periodic 5×5 graphene surface model with 50 C atoms and considered 5 cases:
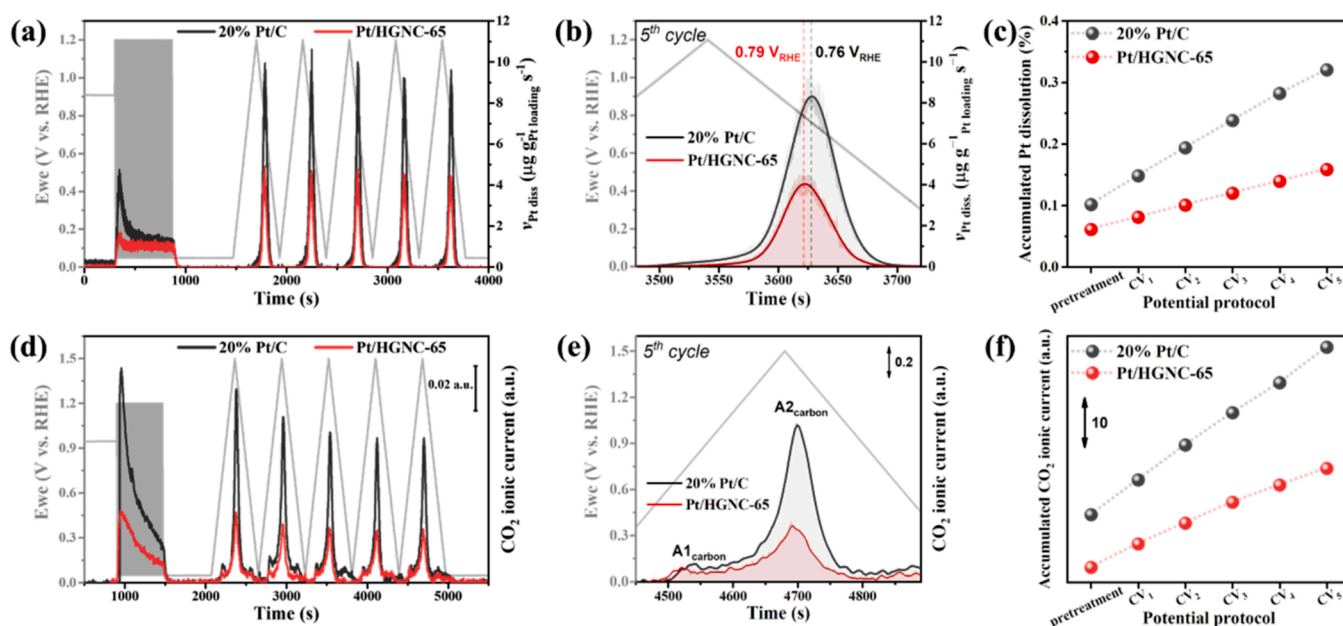

Fig. 6. Online ICP-MS and DEMS analyses. (a, d) Pt dissolution and carbon corrosion results of Pt/C and Pt/HGNC-65. (b, e) Comparison of dissolution and corrosion profiles at the 5th CV cycle. (c, f) Accumulated amount of dissolved Pt and CO_2 evolution ($m/z = 44$) monitored during the overall potential programs investigated. The potential program for monitoring the online Pt dissolution and CO_2 signals consist of 50 fast CV cycles (200 mV s^{-1}) and subsequent 5 slow CV cycles (5 mV s^{-1}) from 0.05 to different UPLs of 1.2 and 1.5 V$_{RHE}$, respectively.
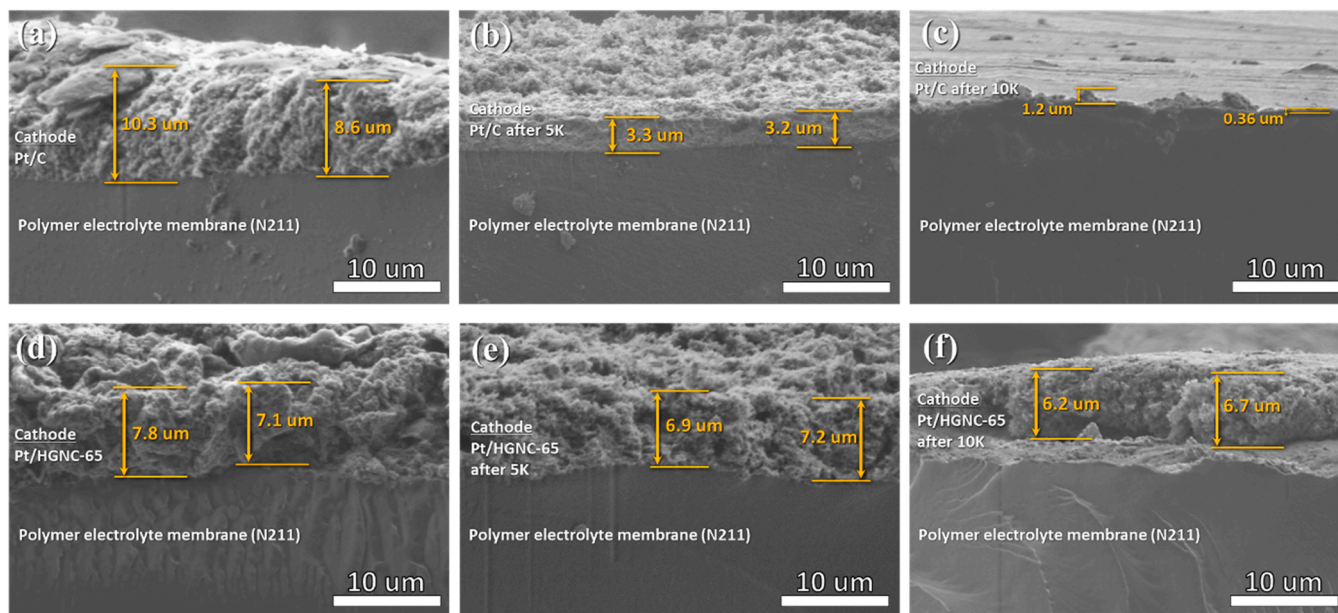
Fig. 7. SEM cross-section of MEAs from commercial Pt/C and Pt/HGNC-65 (a, d) before, (b, e) after 5k, and (c, f) 10 K cycles of catalyst support ADT, respectively. The SEM images were taken from the MEAs after 5 and 10 K ADT polarization tests, respectively.

a. graphene, and nitrogen dopants to create defects
b. pyrrolic-N, Fig. 8dA
c. graphitic-N, Fig. 8dB
d. pyridinic-N, Fig. 8dC

e. pyridinic-N oxide, Fig. 8dD

onto which we attached a Pt13 NP to predict the interaction energetics between Pt NP and N-doped surfaces. This is illustrated in the atomistic pictures of Fig. 8d.
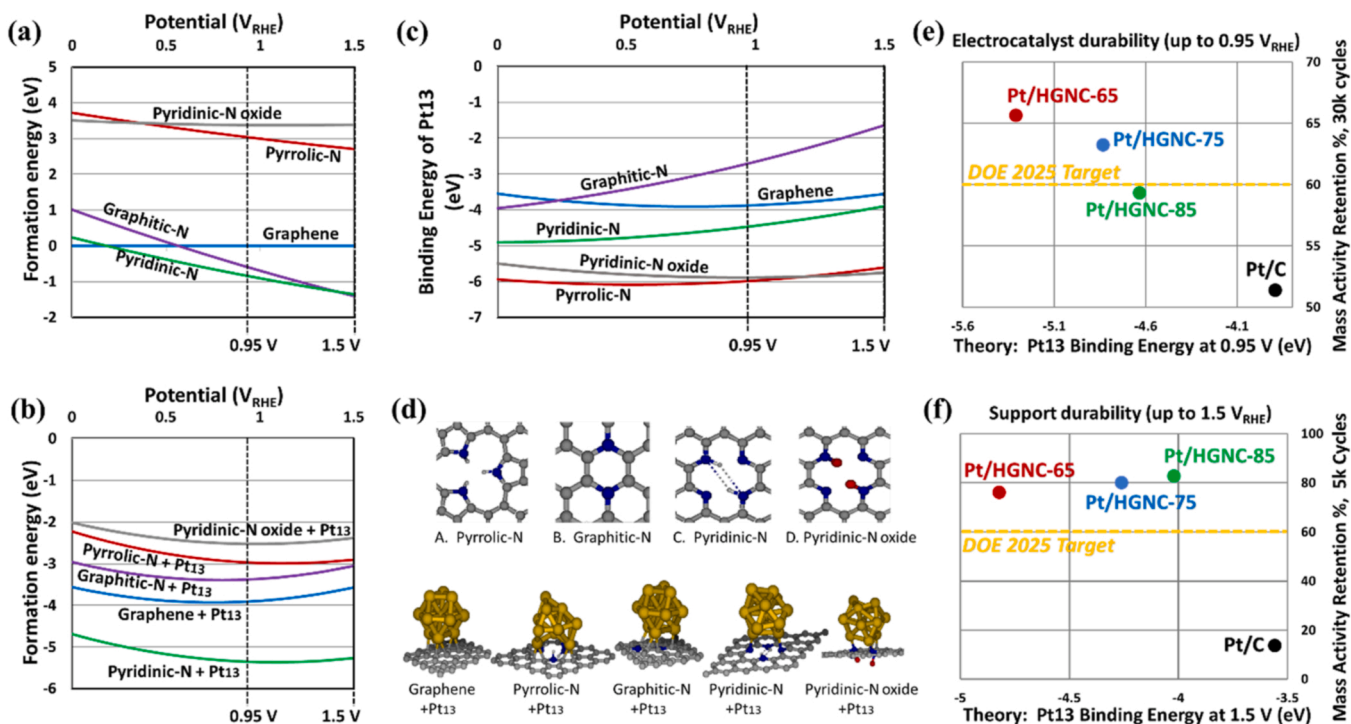

Fig. 8. Formation energies as a function of applied potential V_{RHE} at pH 0 of N-doped graphene defects calculated via the GCP-K grand canonical approach. Here, the QM equilibrium calculations are referenced to a graphene sheet, Pt13, N2, H2, and O2 gas. The formation energy of (a) N-doped graphene and (b) Pt13 on N-doped graphene. (c) Free energy of Pt13 NP binding onto the 5 surface models as a function of applied potential V_{RHE} at pH 0. (d) Schematic atomistic pictures of the calculated structures. Grey - C, blue - N, red - O, gold - Pt, white - H. (e) Catalyst durability from experiment (% mass activity retention after 30 K electrocatalyst ADT) compared to Pt NP/support binding from theory at 0.95 V. (f) Support durability from experiment (% mass activity retention after 5 K electrocatalyst ADT) compared to Pt NP/support binding from theory at 1.5 V. We note that **Pt/HGNC-65 and -75 pass both the electrocatalysis durability and support durability DOE 2025 targets** [29].

To include the effect of water solvent and applied electrode potential, we used the grand-canonical potential kinetics (GCP-K) [32,33]. This is used to predict the free energies as a function of applied potential, U as described in Fig. S24. Using the DFT-based GCP-K approach, we calculated the free energy of formation of pure graphene and of various N-doped configurations as a function of the potential U, as shown in Fig. 8a, b. We find that the least stable defects are pyridinic-N oxide and pyrrolic-N (Fig. 8a). Since the pyrrolic-N group is less thermodynamically favoured, it dominates only in HGNC-65 prepared at the lowest temperature (58.7% pyrrolic).

The free Pt_{13} NP was attached to each of the five surfaces, leading to the optimized structures shown in Fig. 8d. Together with the energies of the five surfaces, we calculated the free energy of binding Pt NP to the surfaces as a function of U, using the formula:

$$NP \quad Binding \quad Energy = E_{Pt_{13}-surface}(U) - E_{Pt_{13}}(U) - E_{surface}(U) \qquad (4)$$

The results are shown in Fig. 8c. We find that the binding energies to the Pt NP are strongest for pyrrolic-N and pyridinic-N oxide defects. As might be expected, the least stable defects in Fig. 8a have the strongest attachment to the Pt NP.

We estimated the binding energy for Pt_{13} NP on HGNC-65, HGNC-75, and HGNC-85 by combining the Pt_{13} NP binding energy for each surface (Fig. 8c), weighted by experimental compositions (Table S3). We used the binding energies of the Pt_{13} NP at 1.5 V_{RHE} to predict the support durability at 1.0–1.5 V and the binding energies of the Pt_{13} NP at 0.95 V to predict the electrocatalyst durability for operation at 0.6–0.95 V_{RHE}.

We expect that a stronger binding energy of the Pt_{13} NP to the support surface will increase the barrier for NP detachment and decrease the rate of agglomeration. Since the Pt_{13} binding energy to the support is weaker at 1.5 V than at 0.95 V for all cases, this agglomeration contributes to the decreased durability at the higher potential cycle life tests. Fig. 8e, f compare the predicted Pt_{13} binding energies on Pt/HGNC-65, Pt/HGNC-75, Pt/HGNC-85, and Pt/C materials to mass activity retention % after the ADT (Tables S5 and S6). The predicted durability along the abscissa in Fig. 8e, f is in excellent agreement with the experimental durability along the ordinate. Pt/HGNC-65 contains the highest percent of pyrrolic N-defects, which leads to the strongest predicted NP binding energy and hence to the best durability.

4. Conclusion

In this study, we developed a highly robust HGNC-65 support (prepared by Mg metal reductive pyrolysis of g-C_3N_4) and demonstrate dramatically enhanced ORR and PEMFC performance for Pt NPs dispersed on it compared to the state-of-the-art commercial Pt/C. Our one-pot synthesis approach is both simple and highly efficient in terms of price and energy. Despite a very low carbonization temperature of 650 °C (in contrast to 2000 °C usually used), we attained high graphiticity, leading to excellent electronic conductivity. Moreover, this low temperature allowed retention of significant N-doping, particularly a high amount of pyrrolic-N, in the graphitic carbon skeleton. This led to exceptional resistance to carbon corrosion that prevents aggregation of Pt NPs during ADT cycles. The HGNC-65 support also possessed the high porosity and large surface area necessary for mass transfer. The superior chemical and physical properties of Pt/HGNC-65 lead to the superior ORR activity and durability in PEMFC single cell tests.

Our QM calculations showed that the better durability of Pt/HGNC-65 is due to the strong binding energy of the Pt NPs to the pyrrolic group which is highest in the Pt/HGNC-65. Our predicted lower stability for the pyrrolic group leads to stronger binding to the Pt NP which leads to less agglomeration and dissolution during cycling in full agreement with online ICP-MS and DEMS measurements for Pt NPs and carbon support. This high pyrrolic concentration has not been observed in previous N-doped carbon supports because they were usually prepared at too high temperature. Our development of the low temperature process makes our materials unique. Most important is that Pt/HGNC-65 and Pt/

HGNC-75 pass both the electrocatalyst durability and support durability DOE 2025 targets. Therefore, we expect that high porosity HGNC-X materials will lead to many other novel applications for electrocatalysis with durable carbon frameworks.

CRediT authorship contribution statement

Ha-Young Lee: Conceptualization, Methodology, Data curation, Investigation, Writing – original draft. **Ted H. Yu:** Software, Data curation, Formal analysis, Investigation, Writing – original draft. **Cheol-Hwan Shin:** Validation, Data curation, Investigation, **Alessandro Fortunelli:** Software, Formal analysis, Investigation. **Sang Gu Ji:** Data curation, Investigation. **Yujin Kim:** Data curation, Investigation. **Tong-Hyun Kang:** Resources, Investigation. **Byong-June Lee:** Data curation, Investigation. **Boris V. Merinov:** Software, Formal analysis, Investigation. **William A. Goddard III:** Project administration, Funding acquisition, Writing – review & editing, Supervision. **Chang Hyuck Choi:** Project administration, Funding acquisition, Writing – review & editing, Supervision. **Jong-Sung Yu:** Conceptualization, Project administration, Funding acquisition, Writing – review & editing, Supervision.

Declaration of Competing Interest

The authors declare that they have no known competing financial interests or personal relationships that could have appeared to influence the work reported in this paper.

Data Availability

Data will be made available on request.

Acknowledgements

Appendix A. Supporting information

Supplementary data associated with this article can be found in the online version at doi:10.1016/j.apcatb.2022.122179.

References

[1] M.K. Debe, Electrocatalyst approaches and challenges for automotive fuel cells, Nature 486 (2012) 43–51, https://doi.org/10.1038/nature11115.

[2] Y.-J. Wang, W. Long, L. Wang, R. Yuan, A. Ignaszak, B. Fang, D.P. Wilkinson, Unlocking the door to highly active ORR catalysts for PEMFC applications: polyhedron-engineered Pt-based nanocrystals, Energy Environ. Sci. 11 (2018) 258–275, https://doi.org/10.1039/c7ee02444d.

[3] J.W. Zhang, Y.L. Yuan, L. Gao, G.M. Zeng, M.F. Li, H.W. Huang, Stabilizing Pt-based electrocatalysts for oxygen reduction reaction: fundamental understanding and design strategies, Adv. Mater. 33 (2021), https://doi.org/10.1002/adma.202006494.

[4] V.R. Stamenkovic, D. Strmcnik, P.P. Lopes, N.M. Markovic, Energy and fuels from electrochemical interfaces, Nat. Mater. 16 (2016) 57–69, https://doi.org/10.1038/nmat4738.

[5] D.A. Cullen, K.C. Neyerlin, R.K. Ahluwalia, R. Mukundan, K.L. More, R.L. Borup, A. Z. Weber, D.J. Myers, A. Kusoglu, New roads and challenges for fuel cells in heavy-duty transportation, Nat. Energy 6 (2021) 462–474, https://doi.org/10.1038/s41560-021-00775-z.

[6] K. Singh, E.B. Tetteh, H.-Y. Lee, T.-H. Kang, J.-S. Yu, Tailor-made Pt catalysts with improved oxygen reduction reaction stability/durability, ACS Catal. 9 (2019) 8622–8645, https://doi.org/10.1021/acscatal.9b01420.

[7] L. Du, V. Prabhakaran, X. Xie, S. Park, Y. Wang, Y. Shao, Low-PGM and PGM-free catalysts for proton exchange membrane fuel cells: stability challenges and

material solutions, Adv. Mater. 33 (2021), e1908232, https://doi.org/10.1002/adma.201908232.

[8] S. Maass, F. Finsterwalder, G. Frank, R. Hartmann, C. Merten, Carbon support oxidation in PEM fuel cell cathodes, J. Power Sources 176 (2008) 444–451, https://doi.org/10.1016/j.jpowsour.2007.08.053.

[9] S. Sui, X. Wang, X. Zhou, Y. Su, S. Riffat, C.-j Liu, A comprehensive review of Pt electrocatalysts for the oxygen reduction reaction: nanostructure, activity, mechanism and carbon support in PEM fuel cells, J. Mater. Chem. A 5 (2017) 1808–1825, https://doi.org/10.1039/c6ta08580f.

[10] T. Zhang, P. Wang, H. Chen, P. Pei, A review of automotive proton exchange membrane fuel cell degradation under start-stop operating condition, Appl. Energy 223 (2018) 249–262, https://doi.org/10.1016/j.apenergy.2018.04.049.

[11] Z. Qiao, S. Hwang, X. Li, C. Wang, W. Samarakoon, S. Karakalos, D. Li, M. Chen, Y. He, M. Wang, Z. Liu, G. Wang, H. Zhou, Z. Feng, D. Su, J.S. Spendelow, G. Wu, 3D porous graphitic nanocarbon for enhancing the performance and durability of Pt catalysts: a balance between graphitization and hierarchical porosity, Energy Environ. Sci. 12 (2019) 2830–2841, https://doi.org/10.1039/c9ee01899a.

[12] H. Zhang, H. Ming, W. Zhang, G. Cao, Y. Yang, Coupled carbonization strategy toward advanced hard carbon for high-energy sodium-ion battery, ACS Appl. Mater. Interfaces 9 (2017) 23766–23774, https://doi.org/10.1021/acsami.7b05687.

[13] Z. Yan, M. Cai, P.K. Shen, Low temperature formation of porous graphitized carbon for electrocatalysis, J. Mater. Chem. 22 (2012) 2133–2139, https://doi.org/10.1039/c1jm14765j.

[14] S.B. Yoon, G.S. Chai, S.K. Kang, J.-S. Yu, K.P. Gierszal, M. Jaroniec, Graphitized pitch-based carbons with ordered nanopores synthesized by using colloidal crystals as templates, J. Am. Chem. Soc. 127 (2005) 4188–4189, https://doi.org/10.1021/ja0423466.

[15] B. Fang, J.H. Kim, M.S. Kim, J.-S. Yu, Hierarchical nanostructured carbons with meso-macroporosity: design, characterization, and applications, Acc. Chem. Res. 46 (2013) 1397–1406, https://doi.org/10.1021/ar300253f.

[16] O.H. Kim, Y.H. Cho, S.H. Kang, H.Y. Park, M. Kim, J.W. Lim, D.Y. Chung, M.J. Lee, H. Choe, Y.E. Sung, Ordered macroporous platinum electrode and enhanced mass transfer in fuel cells using inverse opal structure, Nat. Commun. 4 (2013) 2473, https://doi.org/10.1038/ncomms3473.

[17] L. Lin, N. Miao, G.G. Wallace, J. Chen, D.A. Allwood, Engineering carbon materials for electrochemical oxygen reduction reactions, Adv. Energy Mater. 11 (2021), https://doi.org/10.1002/aenm.202100695.

[18] E. Negro, K. Vezzù, F. Bertasi, P. Schiavuta, L. Toniolo, S. Polizzi, V. Di Noto, Interplay between nitrogen concentration, structure, morphology, and electrochemical performance of PdCoNi "core-shell" carbon nitride electrocatalysts for the oxygen reduction reaction, ChemElectroChem 1 (2014) 1359–1369, https://doi.org/10.1002/celc.201402041.

[19] S. Ott, F. Du, M.L. Luna, T.A. Dao, S. Selve, B.R. Cuenya, A. Orfanidi, P. Strasser, Property-reactivity relations of N-doped PEM fuel cell cathode catalyst supports, Appl. Catal. B-Environ. 306 (2022), https://doi.org/10.1016/j.apcatb.2022.121118.

[20] H. Schmies, E. Hornberger, B. Anke, T. Jurzinsky, H.N. Nong, F. Dionigi, S. Kühl, J. Drnec, M. Lerch, C. Cremers, P. Strasser, Impact of carbon support functionalization on the electrochemical stability of Pt fuel cell catalysts, Chem. Mater. 30 (2018) 7287–7295, https://doi.org/10.1021/acs.chemmater.8b03612.

[21] A. Sinhamahapatra, J.-P. Jeon, J.-S. Yu, A new approach to prepare highly active and stable black titania for visible light-assisted hydrogen production, Energy Environ. Sci. 8 (2015) 3539–3544, https://doi.org/10.1039/c5ee02443a.

[22] A. Sinhamahapatra, J.P. Jeon, J. Kang, B. Han, J.-S. Yu, Oxygen-deficient zirconia (ZrO_{2-x}): a new material for solar light absorption, Sci. Rep. 6 (2016) 27218, https://doi.org/10.1038/srep27218.

[23] J. Chen, Z. Mao, L. Zhang, D. Wang, R. Xu, L. Bie, B.D. Fahlman, Nitrogen-deficient graphitic carbon nitride with enhanced performance for lithium ion battery anodes, ACS Nano 11 (2017) 12650–12657, https://doi.org/10.1021/acsnano.7b07116.

[24] Y.W. Ding, C. Yu, J.W. Chang, C. Yao, J.H. Yu, W. Guo, J.H. Qiu, Effective fixation of carbon in g-C_3N_4 enabled by mg-induced selective reconstruction, Small 16 (2020), https://doi.org/10.1002/smll.201907164.

[25] H. Li, H.-Y. Lee, G.-S. Park, B.-J. Lee, J.-D. Park, C.-H. Shin, W. Hou, J.-S. Yu, Conjugated polyene-functionalized graphitic carbon nitride with enhanced photocatalytic water-splitting efficiency, Carbon 129 (2018) 637–645, https://doi.org/10.1016/j.carbon.2017.12.048.

[26] B. Fang, N.K. Chaudhari, M.S. Kim, J.H. Kim, J.-S. Yu, Homogeneous deposition of platinum nanoparticles on carbon black for proton exchange membrane fuel cell, J. Am. Chem. Soc. 131 (2009) 15330–15338, https://doi.org/10.1021/ja905749e.

[27] D.S. Yang, M.Y. Song, K.P. Singh, J.-S. Yu, The role of iron in the preparation and oxygen reduction reaction activity of nitrogen-doped carbon, Chem. Commun. 51 (2015) 2450–2453, https://doi.org/10.1039/c4cc08592b.

[28] T.J. Schmidt, H.A. Gasteiger, G.D. Stab, P.M. Urban, D.M. Kolb, R.J. Behm, Characterization of high-surface area electrocatalysts using a rotating disk electrode configuration, J. Electrochem. Soc. 145 (1998) 2354–2358, https://doi.org/10.1149/1.1838642.

[29] U.S. Department of Energy (DOE) Fuel Cell Technologies Office, (FCTO) Fuel Cells Multi-Year Research Development and Demonstration Plan, Table P.1 and P.2. ⟨www.energy.gov/sites/prod/files/2016/06/f32/fcto_myrdd_fuel_cells_0.pdf⟩, 2016 (accessed 18 June 2022).

[30] S. Grimme, J. Antony, S. Ehrlich, H. Krieg, A consistent and accurate ab initio parametrization of density functional dispersion correction (DFT-D) for the 94 elements H-Pu, J. Chem. Phys. 132 (2010), 154104, https://doi.org/10.1063/1.3382344.

[31] J.P. Perdew, K. Burke, M. Ernzerhof, Generalized gradient approximation made simple, Phys. Rev. Lett. 77 (1996) 3865–3868, https://doi.org/10.1103/PhysRevLett.77.3865.

[32] Y. Huang, R.J. Nielsen, W.A. Goddard 3rd, Reaction mechanism for the hydrogen evolution reaction on the basal plane sulfur vacancy site of MoS_2 using grand canonical potential kinetics, J. Am. Chem. Soc. 140 (2018) 16773–16782, https://doi.org/10.1021/jacs.8b10016.

[33] M.D. Hossain, Y. Huang, T.H. Yu, W.A. Goddard III, Z. Luo, Reaction mechanism and kinetics for CO_2 reduction on nickel single atom catalysts from quantum mechanics, Nat. Commun. 11 (2020) 2256, https://doi.org/10.1038/s41467-020-16119-6.

[34] P.A. Schultz, Local electrostatic moments and periodic boundary conditions, Phys. Rev. B 60 (1999) 1551–1554, https://doi.org/10.1103/PhysRevB.60.1551.

[35] P.A. Schultz, SEQQUEST, dft.sandia.gov/Quest/, (accessed 18 June 2022).

[36] R. Sundararaman, W.A. Goddard 3rd, The charge-asymmetric nonlocally determined local-electric (CANDLE) solvation model, J. Chem. Phys. 142 (2015), 064107, https://doi.org/10.1063/1.4907731.

[37] R. Sundararaman, jDFTx, jdftx.org, (accessed 18 June 2022).

[38] Y.F. Hao, Y.Y. Wang, L. Wang, Z.H. Ni, Z.Q. Wang, R. Wang, C.K. Koo, Z.X. Shen, J. T.L. Thong, Probing layer number and stacking order of few-layer graphene by Raman spectroscopy, Small 6 (2010) 195–200, https://doi.org/10.1002/smll.200901173.

[39] H. Wang, T. Maiyalagan, X. Wang, Review on recent progress in nitrogen-doped graphene: synthesis, characterization, and its potential applications, ACS Catal. 2 (2012) 781–794, https://doi.org/10.1021/cs200652y.

[40] J. Liu, P. Song, W.L. Xu, Structure-activity relationship of doped-nitrogen (N)-based metal-free active sites on carbon for oxygen reduction reaction, Carbon 115 (2017) 763–772, https://doi.org/10.1016/j.carbon.2017.01.080.

[41] C.V. Rao, C.R. Cabrera, Y. Ishikawa, In search of the active site in nitrogen-doped carbon nanotube electrodes for the oxygen reduction reaction, J. Phys. Chem. Lett. 1 (2010) 2622–2627, https://doi.org/10.1021/jz100971v.

[42] E.G. Luo, M.L. Xiao, J.J. Ge, C.P. Liu, W. Xing, Selectively doping pyridinic and pyrrolic nitrogen into a 3D porous carbon matrix through template-induced edge engineering: enhanced catalytic activity towards the oxygen reduction reaction, J. Mater. Chem. A 5 (2017) 21709–21714, https://doi.org/10.1039/c7ta07608h.

[43] W. Ding, Z.D. Wei, S.G. Chen, X.Q. Qi, T. Yang, J.S. Hu, D. Wang, L.J. Wan, S. F. Alvi, L. Li, Space-confinement-induced synthesis of pyridinic- and pyrrolic-nitrogen-doped graphene for the catalysis of oxygen reduction, Angew. Chem. Int. Ed. 52 (2013) 11755–11759, https://doi.org/10.1002/anie.201303924.

[44] R. Sharma, S. Gyergyek, S.M. Andersen, Critical thinking about baseline corrections for electrochemical surface area (ECSA) determination of Pt/C through H-adsorption/H-desorption regions of a cyclic voltammogram, Appl. Catal. B-Environ. 311 (2022), https://doi.org/10.1016/j.apcatb.2022.121351.

[45] M. Lopez-Haro, L. Dubau, L. Guetaz, P. Bayle-Guillemaud, M. Chatenet, J. Andre, N. Caque, E. Rossinot, F. Maillard, Atomic-scale structure and composition of Pt_3Co/C nanocrystallites during real PEMFC operation: A STEM-EELS study, Appl. Catal. B-Environ. 152 (2014) 300–308, https://doi.org/10.1016/j.apcatb.2014.01.034.

[46] P.P. Lopes, D. Li, H. Lv, C. Wang, D. Tripkovic, Y. Zhu, R. Schimmenti, H. Daimon, Y. Kang, J. Snyder, N. Becknell, K.L. More, D. Strmcnik, N.M. Markovic, M. Mavrikakis, V.R. Stamenkovic, Eliminating dissolution of platinum-based electrocatalysts at the atomic scale, Nat. Mater. 19 (2020) 1207–1214, https://doi.org/10.1038/s41563-020-0735-3.

[47] S.W. Lee, S.R. Choi, J. Jang, G.-G. Park, S.H. Yu, J.-Y. Park, Tolerance to carbon corrosion of various carbon structures as catalyst supports for polymer electrolyte membrane fuel cells, J. Mater. Chem. A 7 (2019) 25056–25065, https://doi.org/10.1039/c9ta07941f.

[48] P. Kanninen, B. Eriksson, F. Davodi, M.E.M. Buan, O. Sorsa, T. Kallio, R. W. Lindström, Carbon corrosion properties and performance of multi-walled carbon nanotube support with and without nitrogen-functionalization in fuel cell electrodes, Electrochim. Acta 332 (2020), https://doi.org/10.1016/j.electacta.2019.135384.

[49] Q. Meyer, Y.C. Zeng, C. Zhao, In situ and operando characterization of proton exchange membrane fuel cells, Adv. Mater. 31 (2019), https://doi.org/10.1002/adma.201901900.

[50] R. Sharma, S.M. Andersen, An opinion on catalyst degradation mechanisms during catalyst support focused accelerated stress test (AST) for proton exchange membrane fuel cells (PEMFCs), Appl. Catal. B-Environ. 239 (2018) 636–643, https://doi.org/10.1016/j.apcatb.2018.08.045.

[51] P. Jovanovic, U. Petek, N. Hodnik, F. Ruiz-Zepeda, M. Gatalo, M. Sala, V.S. Selih, T. P. Fellinger, M. Gaberscek, Importance of non-intrinsic platinum dissolution in Pt/C composite fuel cell catalysts, Phys. Chem. Chem. Phys. 19 (2017) 21446–21452, https://doi.org/10.1039/c7cp03192k.

[52] L. Castanheira, W.O. Silva, F.H.B. Lima, A. Crisci, L. Dubau, F. Maillard, Carbon corrosion in proton-exchange membrane fuel cells: effect of the carbon structure, the degradation protocol, and the gas atmosphere, ACS Catal. 5 (2015) 2184–2194, https://doi.org/10.1021/cs501973j.

[53] L. Castanheira, L. Dubau, M. Mermoux, G. Berthome, N. Caque, E. Rossinot, M. Chatenet, F. Maillard, Carbon corrosion in proton-exchange membrane fuel cells: from model experiments to real-life operation in membrane electrode assemblies, ACS Catal. 4 (2014) 2258–2267, https://doi.org/10.1021/cs500449q.

[54] R. Borup, K. More, A. Weber, Fuel Cell Performance and Durability Consortium, US DOE Annual Merit Review Proceedings, https://www.hydrogen.energy.gov/pdfs/review18/fc135_borup_2018_o.pdf, 2018 (accessed 18 June 2022).